

Secondary Gravity Waves Generated by Breaking Mountain Waves over Europe

C. J. Heale¹, K. Bossert², S. L. Vadas³, L. Hoffmann⁴, A. Dörnbrack⁵, G. Stober⁶, J. B. Snively¹, C. Jacobi⁷

¹Center for Space and Atmospheric Research (CSAR), Embry-Riddle Aeronautical University, 600 S.

Clyde Morris Blvd, Daytona Beach, FL 32114, USA

²University of Alaska, Fairbanks, 1760 Tanana Loop, Fairbanks, AK, 99775, USA

³NorthWest Research Associates, Inc., 3380 Mitchell Lane, Boulder, CO 80301, USA

⁴Jülich Supercomputing Centre, Forschungszentrum Jülich, Jülich, Germany

⁵DLR, Institut für Physik der Atmosphäre, D-82230 Oberpfaffenhofen

⁶University of Bern, Institute of Applied Physics, Sidlerstrasse 5, CH-3012 Bern, Switzerland

⁷University of Leipzig, Institute for Meteorology, Stephanstr. 3, D-041032 Leipzig, Germany

Key Points:

- Mountain wave breaking in the MLT couples directly to secondary waves
- Tidal winds act like a filter for secondary wave spectra reaching the thermosphere
- Non-primary wave forcing is significant and distribution is governed by thermospheric winds

Abstract

A strong mountain wave, observed over Central Europe on the 12th Jan 2016, is simulated in 2D under 2 fixed background wind conditions representing opposite tidal phases. The aim of the simulation is to investigate the breaking of the mountain wave and subsequent generation of non-primary waves in the upper atmosphere. The model results show that the mountain wave first breaks as it approaches a mesospheric critical level creating turbulence on horizontal scales of 8-30km. These turbulence scales couple directly to horizontal secondary waves scales, but those scales are prevented from reaching the thermosphere by the tidal winds which act like a filter. Initial secondary waves which can reach the thermosphere range from 60-120km in horizontal scale and are influenced by the scales of the horizontal and vertical forcing associated with wave breaking at mountain wave zonal phase width, and horizontal wavelength scales. Large scale non-primary waves dominate over the whole duration of the simulation with horizontal scales of 107-300km and periods of 11-22 minutes. The thermosphere winds heavily influence the time-averaged spatial distribution of wave forcing in the thermosphere, which peaks at 150km altitude and occurs both westward and eastward of the source in the 2 UT background simulation and primarily eastward of the source in the 7 UT background simulation. The forcing amplitude is $\sim 2\times$ that of the primary mountain wave breaking and dissipation. This suggests that non-primary waves play a significant role in gravity waves dynamics and improved understanding of the thermospheric winds is crucial to understanding their forcing distribution.

1 Introduction

Gravity Waves (GWs) play an important role in the transport of energy and momentum from the lower to the middle and upper atmosphere (e.g. Fritts & Alexander, 2003; Garcia & Solomon, 1985; Holton, 1982; Lindzen, 1981; Vadas, Liu, & Lieberman, 2014; Yiğit & Medvedev, 2015). Through dissipation mechanisms such as viscosity, critical level filtering, and wave breaking, waves can deposit their energy and momentum into the mean state causing localized forcing of the mean winds and heating/cooling of the atmosphere (Fritts & Alexander, 2003; Heale, Snively, Hickey., & Ali, 2014; Heale, Walterscheid, & Snively, 2018; Hickey, Walterscheid, & Schubert, 2011; Holton, 1983; Holton & Alexander, 2000; Lund & Fritts, 2012; McFarlane, 1987; Vadas, 2007; Vadas & Fritts, 2005; Vadas, Fritts, & Alexander, 2003). The influence of gravity wave forc-

ing contributes to atmospheric phenomena such as the Quasi-Biennial Oscillation (QBO) (Alexander & Holton, 1997; Baldwin et al., 2001; Dunkerton, 1997; Ern et al., 2014; Piani, Durran, Alexander, & Holton, 2000), the summer branch of the Brewer-Dobson circulation (Alexander & Rosenlof, 2003; Stephan, Alexander, & Richter, 2016), and the cold summer mesopause (Alexander & Rosenlof, 1996; Garcia & Solomon, 1985; Holton & Alexander, 2000) amongst others.

One important source of gravity wave generation is via flow over topography (also known as orographic or mountain waves) (Bacmeister, 1993; Dörnbrack, Leutbecher, Kivi, & Kyro, 1999; Durran & Klemp, 1987; McFarlane, 1987; McLandress, Shepherd, Polavarapu, & Beagley, 2012; Nastrom & Fritts, 1992; R. B. Smith, 1979). The lifting of surface level winds as it flows over the terrain leads to the generation of quasi-stationary waves (approximately zero relative ground period) that propagate upwards into the atmosphere (Nappo, 2002). Hotspots for such waves exist over mountainous regions of the world such as the South American Andes, the European alps and Scandinavian mountains, New Zealand, and Antarctica (Hoffmann, Xue, & Alexander, 2013) where the flow near the mountain tops are approximately perpendicular to the mountain range. A unique feature of these mountain waves is that they can only exist in the presence of a mean background wind. If the mountain wave encounters a region of zero wind, the layer acts as a critical level, and filters the wave into the mean flow (Booker & Bretherton, 1967). In the summertime, winds switch between east and westward directions in the middle atmosphere, thus, mountain waves tend to get filtered in the stratosphere. However, in the wintertime, the winds do not typically reverse sign until the mesosphere and, thus, mountain waves can propagate up to these altitudes and obtain larger amplitudes before being filtered. As such, mountain waves tend to dominate in the wintertime (Hoffmann et al., 2013). As the mountain wave approaches the critical level, it is refracted to smaller vertical scale. The smaller vertical scale, at large amplitudes, lead to large vertical gradients in the wind and temperature structure of the wave which can cause the mountain wave to break. The wave breaking creates turbulence and generates secondary acoustic-gravity waves (Bacmeister & Schoeberl, 1989; Bossert et al., 2017; Ehard et al., 2016; Heale et al., 2017; Sato-mura & Sato, 1999; S. M. Smith, Vadas, Baggaley, Hernandez, & Baumgardner, 2013; Vadas, Zhao, Chu, & Becker, 2018).

Secondary gravity waves are categorized by two mechanism: linear and nonlinear generation (furthermore referred to as non-primary waves since the dissipation and new

wave generation process can happen multiple times). The linear mechanism arises as a primary wave dissipates as a whole. The dissipation exerts a body force on the mean flow at packet scale, which generates a spectra of non-primary waves with larger scales and longer periods than the primary wave. The theory for these waves is described in Vadas et al. (2003, 2018) and such waves have been identified over Antarctica via identifying characteristic fishbone patterns in lidar data and simulation results. In contrast, the non-linear mechanism is associated wave breaking and the cascade to smaller scales (e.g. Achatz, 2007; Andreassen, Wasberg, Fritts, & Isler, 1994; Bacmeister & Schoeberl, 1989; Dörnbrack, 1998; Franke & Robinson, 1999; Fritts, Wang, Werne, Lund, & Wan, 2009; Horinouchi, Nakamura, & Kosaka, 2002; Lund & Fritts, 2012; Satomura & Sato, 1999; J. Snively & Pasko, 2003). The theory being that breaking produces localized forcing at the turbulent scales and periods, which generate nonprimary gravity waves (Chun & Kim, 2008; Y.-H. Kim & Chun, 2008; Song, Chun, & Lane, 2003; Zhou, Holton, & Mullendore, 2002). As such, these non-primary waves are expected to have scales and periods that are smaller than those of the primary breaking wave. There is debate however, over the dominance and importance of each mechanism.

The DEEPWAVE campaign (e.g. Fritts et al., 2015) used coordinated observations and modeling to study the propagation of mountain waves over New Zealand from the ground to the thermosphere (e.g. Bossert et al., 2015; Bramberger et al., 2017; Eckermann et al., 2016; N. Kaifler et al., 2017; R. B. Smith et al., 2016). The campaign found that there was often a multi-scale wave environment in the mesosphere within the phases of a larger scale mountain wave (Bossert et al., 2015). Further studies suggested that the mountain wave would break in the mesosphere, generating quasi-stationary eddy structures and propagating non-primary waves. Observation techniques, such as airglow imaging, make it difficult to identify the difference between the turbulent and non-primary wave structures because it measures integrated values over a layer. However, turbulent and wave structures were identified in height dependent lidar data (Bossert et al., 2017; Heale et al., 2017). The campaign revealed that mesospheric activity and wave breaking was present on days where surface wind forcing was small. If the surface wind forcing was too large the mountain wave would break in the stratosphere, due to having a large amplitude, and would dissipate before reaching the mesosphere (Ehard et al., 2017; Fritts et al., 2018; B. Kaifler et al., 2015). Despite significant advancement, very little is still known about the spectra and importance of non-primary waves in the upper at-

mosphere. Most General Circulation Models (GCMs) are hydrostatic and only resolve inertia gravity waves which have long periods and act in an incompressible manner. Smaller wavelength, shorter period Acoustic Gravity Waves (AGWs), which can require compressible effects, have to be parameterized in these models (Y. J. Kim, Eckermann, & Chun, 2003). Non-primary waves can re-populate parts of the phase speed spectrum which have encountered a critical level below. Thus, we could miss important physics which cannot be described by tropospheric sources. Therefore, their study remains an important topic in advancing our understanding of the effects of GWs on the atmosphere as a whole.

In this paper, we use the time-dependent, fully nonlinear, high-resolution numerical model, known as MAGIC (Model for Acoustic and Gravity wave Interactions in a Compressible atmosphere) (J. B. Snively, 2013; J. B. Snively & Pasko, 2008; Zettergren & Snively, 2015) to simulate a mountain wave from the ground to 300km altitude, in 2D. The simulation is based upon a mountain wave observed over Central Europe on the 12th January 2016. In particular, we focus on the nonlinearity, wave breaking, and non-primary wave generation of the mountain wave in the mesosphere and thermosphere regions of the atmosphere assuming two different solar tidal phases. We aim to elucidate the coupling mechanisms and spectra of non-primary waves generated by the breaking mountain wave. The paper is structured as follows: Section 2 presents the observations and mesoscale modeling of the mountain wave, section 3 presents the numerical model and simulation set-up, section 4 presents the results of the simulations, and section 5 serves as summary and conclusions.

2 Observed Mountain Wave

A strong mountain wave was observed by the Atmosphere InfraRed Sounder (AIRS) instrument (Aumann et al., 2003) over Central Europe on the 12th January of 2016. A high-resolution temperature retrieval for this case was obtained using the approach of Hoffmann and Alexander (2009). The AIRS retrieval results at $z=36\text{km}$ are displayed in Figure 1a and show the wave predominately over the European alps between 5-10 degrees east and 40-50 degrees north with a horizontal wavelength of $\sim 230\text{ km}$. A temperature cross-section, along the red line in Figure 1a, is shown in Figure 1c. The retrieval yielded a wave amplitude of 25 K in the stratosphere and lower mesosphere and a vertical wavelength of $\sim 20\text{ km}$. One hourly operational analyses and short-term forecasts of the European Centre for Medium-Range Weather Forecasting (ECMWF) provided

mesoscale and large-scale modeling results of the event. The integrated forecast system (IFS) of the ECMWF is a global NWP model solving the hydrostatic primitive equations. The horizontal resolution of the IFS cycle used for this study is about 9 km (Hólm, Forbes, Lang, Magnusson, & Malardel, 2016; Malardel & Wedi, 2016). Ehard et al. (2018) analyzed ground-based lidar measurements from December 2015 and showed that the IFS data give reliable gravity wave amplitudes up to about 40 - 50 km altitude. During the same period, the phase and location of mountain-wave induced polar stratospheric clouds above Svalbard was very well simulated (Dörnbrack, Gisinger, Pitts, Poole, & Maturilli, 2017).

Temperature perturbations calculated in a similar manner as for AIRS observations found the presence of a mountain wave with similar amplitudes and wavelengths to the AIRS observation (Figure 1c and d). Both showed large temperature enhancements associated with the presence of the stratospheric jet-stream to the north of the mountain wave over the United Kingdom and Scandinavia. The IFS data suggest the jet-stream causes a refraction of the mountain wave phases from the north-south to the east-west direction, since the horizontal wind is larger north of the wave event. The observation and modeling results, however, do not capture the significant wave nonlinearity and breaking that would be expected from such a strong wave in the Mesosphere and Lower Thermosphere (MLT) region. Therefore, the MAGIC model is used to simulate the mountain wave, along the red line (at 47 N), from the ground up to 300 km altitude in order to examine the breaking processes and non-primary wave generation associated with this mountain wave event in the upper atmosphere.

3 Numerical Model

The numerical model, used for the simulations, is a 2D version of the time-dependent, high-resolution numerical model, known as MAGIC (J. B. Snively, 2013; J. B. Snively & Pasko, 2008; Zettergren & Snively, 2015). The numerical model solves the nonlinear, fully compressible Euler equations, with gravity as a balanced source term, and Navier Stokes viscosity (J. B. Snively, 2013; J. B. Snively & Pasko, 2008). This is done using an adaptation of the Clawpack routines [www.clawpack.org], which solve a hyperbolic system of equations using a finite volume approach (LeVeque, 2002; LeVeque & Berger, 2004). The model decomposes flux differences between cell boundaries into characteristic ‘f-waves’ (Bale, LeVeque, Mitran, & Rossmannith, 2002), each of which propagate

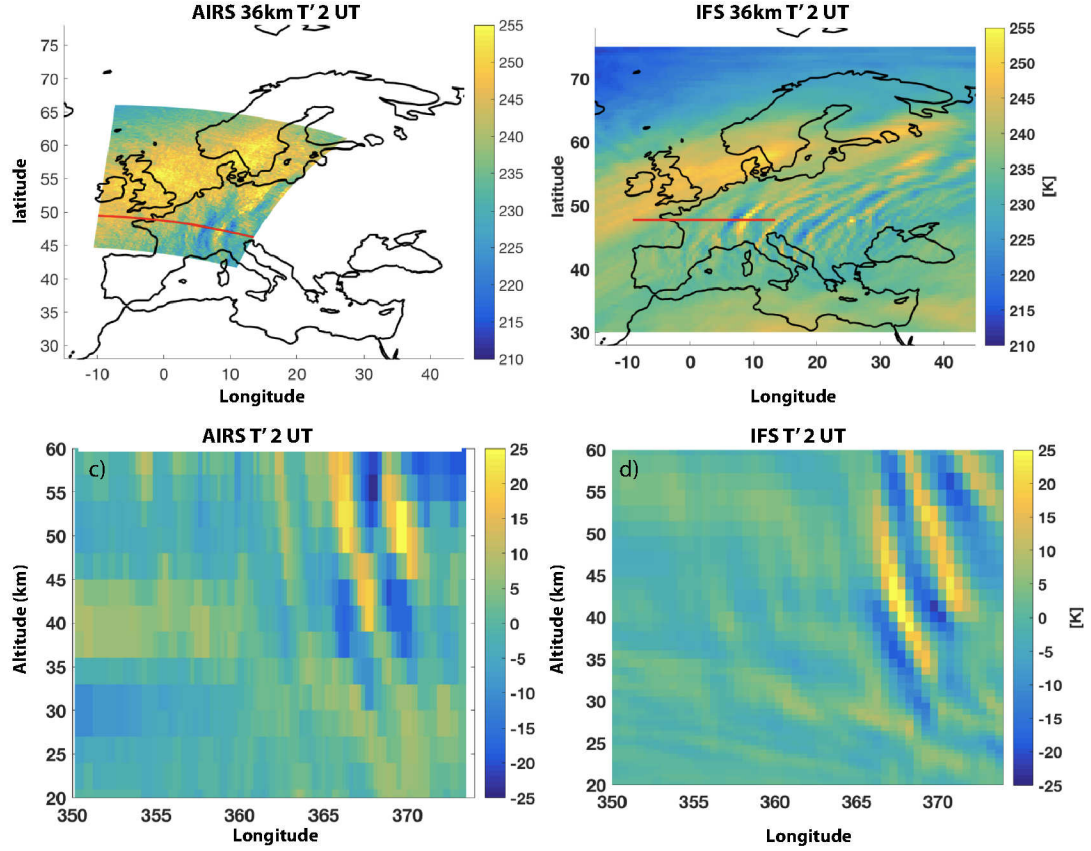


Figure 1. Observations and mesoscale modeling of a mountain wave over Europe on 12th January 2016 for (a) and (b) the AIRS and IFS temperature data at $z=36$ km altitude and (c) and (d) a zonal slice of T' along the red line in the stratosphere.

at characteristic speeds. The model accounts for dissipation due to molecular viscosity and thermal conduction and solves for these using a time-split method.

3.1 Wave forcing and simulation domain

The mountain wave is excited using the simplified source used in Heale et al. (2017) which represents the wave as a vertical body forcing with a fixed horizontal phase. Tests were run using a topographic source, but low frequency modes with long horizontal wavelengths were generated that interfered with the side boundary and didn't contribute to the solution in the upper atmosphere (our region of interest). Therefore, the simplified source was used. The vertical body forcing is specified as follows:

$$F(x, z, t) = A \cdot \rho \cdot \cos[k(x - x_c)] \cdot \exp \left[-\frac{(z - z_c)^2}{2\sigma_z^2} - \frac{(x - x_c)^2}{2\sigma_x^2} - \frac{(t - t_c)^2}{2\sigma_t^2} \right] \quad (1)$$

where $A=0.1 \text{ m/s}^2$, ρ is the density, k is the horizontal wavenumber ($2\pi/230\text{km}$), $z_c=10\text{km}$, $\sigma_z=3\text{km}$, $x_c=1500 \text{ km}$, $\sigma_x=230\text{km}$, $t_c=6\text{hrs}$, and $\sigma_t=1.5\text{hrs}$. The vertical half-width is chosen to be large enough to generate a coherent gravity wave, and not so large that the ambient atmospheric conditions vary too rapidly over that scale. The temporal half-width is chosen to ramp the wave up slowly enough that the forcing does not produce large transients. The horizontal wavelength was chosen from the wavelength measured in the AIRS image (230 km). It is noted that IFS applies a sponge layer that artificially decreases amplitudes above $\sim 40\text{km}$ altitude. In addition, the AIRS retrieval algorithm uses a series of weighting functions at different altitudes (Hoffmann & Alexander, 2009) which also underestimate amplitudes, especially above $\sim 50\text{km}$ and for waves with short vertical wavelengths. As such, the forcing amplitude was chosen to best match the AIRS and IFS amplitudes in the stratosphere at 40km where we have more confidence in their accuracy. The simulation domain was chosen to represent a zonal slice at a latitude of 47 degrees north, corresponding to the strongest portion of the wave in Figure 1. The horizontal domain is 3000km in zonal extent with a horizontal resolution of 1km . The vertical domain ranges from the ground to 300km altitude with 250m resolution. The simulation was run for 9 hours, with frames output every 2.5 minutes. The side and top boundary conditions are open, the bottom boundary is closed (reflective), and a sponge layer is applied to the top 30km of the domain.

3.2 Background atmosphere

The simulation requires a fixed background ambient atmosphere for the excited mountain wave to propagate through. However, the tidal phase would change significantly over the 9 hour period of the simulation. Therefore, two simulations are run with opposing tidal phases to ascertain some of the differences that would arise from the changing tide that is not captured in the model. The two simulations are named the 2 UT and 7 UT simulations as these represent the times at which the background atmospheric profile was chosen. The atmospheric background zonal winds and temperatures are obtained from the IFS atmospheric states for $z=0-60\text{km}$ altitude. The meteor radar at Collm, Germany (51.30N, 13.02 E) (Jacobi, 2012; Stober et al., 2017) was used to represent the winds between 70-100 km and captures the tidal phases (Stober, Chau, Vierinen, Jacobi, & Wilhelm, 2018), and the HWM07 model (Drob et al., 2008) was used for the winds above 100km and between 60-70km. The temperature and densities were taken from NRLMSISE-00 model (Picone, Hedin, Drob, & Aikin, 2002). The zonal wind profiles for the 2 UT and 7 UT simulations are shown in Figure 2a, with the Collm Meteor Radar (MR) winds shown in Figure 2b.

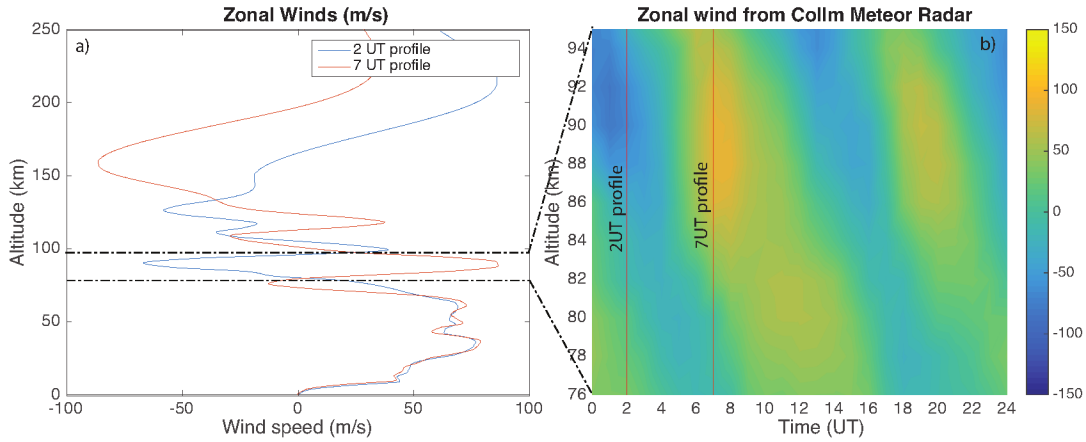


Figure 2. a) Zonal wind profiles used as background atmospheric conditions for the 2 UT and 7 UT simulations, and b) the Collm Meteor Radar data (m/s) for the 12th January 2016.

Figure 2a indicates that the lower atmospheric winds (0-60km) show little variation between 2 and 7 UT, but have opposing tidal phases between 70-100km altitude (westward at 2 UT and eastward at 7 UT). The eastward tide in the 7 UT simulation has a

larger magnitude than the westward tide at 2 UT by ~ 20 m/s. The thermospheric winds are also significantly different at 2 and 7 UT with the winds predominantly eastward at 2 UT (peaking at 210 km altitude) and westward at 7 UT (peaking at 160 km altitude).

4 Effects of atmospheric wind and temperature on waves

In order to understand the discussion in the results section, a brief description of the effects of winds and temperature structure on waves. Horizontal winds and temperature structure that vary in altitude refract a wave by changing the vertical wavelength. If the wind increases in the direction of wave propagation, then the wave's vertical wavelength is decreased and the wave's trajectory becomes more horizontal; a positive temperature gradient with altitude will have the same effect. If the wind increases in the opposite direction of the wave propagation, the vertical wavelength is increased and the wave's trajectory becomes more vertical; a negative temperature gradient with altitude will have the same effect. If the wind is in the same direction as the wave and increases to the point where its magnitude matches the horizontal phase speed of a wave, the vertical wavelength approaches zero and the wave is absorbed into the mean flow (a critical level). Often times, if the wave is of sufficient amplitude, the refraction to small vertical scales leads to large vertical shears in the wave itself which can cause the wave to break as it approaches a critical level. If the winds and temperature structures vary such that the wave's intrinsic frequency becomes equal to the local buoyancy frequency, then the wave will undergo partial or total reflection. The region above the reflection layer is known as an evanescent region (region where the buoyancy period exceeds the wave period), where the wave solution decays exponentially with altitude. However, with sufficient amplitude, the wave can tunnel through the evanescent layer and continue propagating above the upper edge of the layer. In the context of these simulations, the strong tidal winds can act as a critical or evanescent layer for certain wave modes, depending upon the wave parameters and their direction of propagation. Therefore, the tidal phase shown in Figure 2b has the ability to control the spectrum of waves that can propagate into the upper regions of the thermosphere.

5 Results

5.1 Comparison with AIRS and IFS

Figure 3 shows a comparison of the zonal-altitude slice at 47 degrees north in the AIRS observation, MAGIC simulation, and the IFS. The MAGIC model (Figure 3b), even with the simplified source, captures the amplitudes and vertical phase structure of the mountain wave well when compared to Figure 3a and c. As previously noted, the MAGIC amplitudes were chosen so that they match well with IFS and AIRS at 40km altitude. Above this altitude, the IFS and AIRS results may underestimate the true amplitude of the wave due to sponge layer damping and larger uncertainties in the retrieval algorithms respectively. However, tests with MAGIC suggest that the wave is already close to saturation at the amplitude shown in Figure 3b. Increasing the amplitude of the forcing even more will lead to increased linearities and harmonic generation but won't impact the primary wave amplitudes much. Making this comparison gives us confidence 1) in using the simplified source and 2) that the results in the MLT are a fair representation of the actual dynamics that would occur in 2D. Note that amplitudes and breaking dynamics would be different in 3D and will be examined in a future paper.

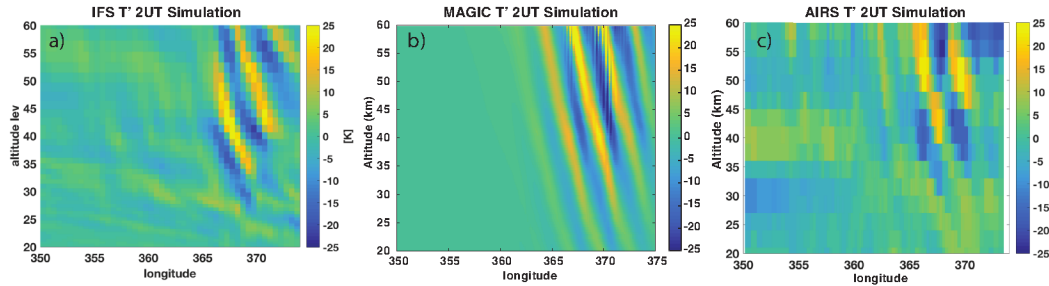


Figure 3. Comparison of the zonal-altitude slices for the a) IFS, b) MAGIC, and c) AIRS temperature perturbations in the stratosphere (K).

5.2 Wave evolution

Figure 4 shows the temperature perturbation field, for both the 2 UT (a-c) and 7 UT (d-f) simulations, at $t=5.83$, 6.6 and 7.5 hours into the simulation. At $t=5.83$ hours (panels a and d), the mountain wave can be seen clearly in the lower and middle atmosphere but does not propagate above the red dotted line, which represents the lowest al-

270 titude that the zonal wind crosses zero. The point where the zonal wind (represented
 271 by the blue line in Figure 4) crosses zero is a critical level for mountain waves (since a
 272 stationary mountain wave possesses a zero ground-relative phase speed). As the moun-
 273 tain wave approaches the critical level, the decreasing wind causes the vertical wavelength
 274 of the wave to decrease in tandem. The decreased vertical wavelength leads to larger ver-
 275 tical gradients in the wave fields, which can cause a wave to break as it approaches the
 276 critical level. Since the lowest critical level exists at 80 km for the 2 UT simulation and
 277 73 km in the 7 UT simulation, The mountain wave can propagate higher before it is likely
 278 to break in the 2 UT case. It also means that the horizontal phase structure is differ-
 279 ent at the altitude the wave breaks in the 2 and 7 UT cases.

280 At $t=6.6$ hours (Figures 4b and e), the mountain wave breaks into smaller struc-
 281 ture above ~ 60 km as it approaches the critical level (indicated by the red dotted line)
 282 and the vertical gradients in the wave become large enough to cause instability. Due to
 283 the phase progression between the different breaking altitudes in the 2 and 7 UT sim-
 284 ulations, the mountain wave breaks along two wavefronts in the 2 UT simulation (Fig-
 285 ures 4b), and 3 wave fronts in the 7 UT simulation (Figures 4e). The breaking is most
 286 prominent in the warm phase of the wave as instability conditions are more likely to be
 287 met here (see Heale et al. (2017) for more detail). Non-stationary non-primary waves are
 288 present above ~ 100 km altitude in both Figures 4b and e (see supporting information
 289 for the movie), generated by the breaking of the mountain wave. In Figures 4b, there
 290 are two very distinct packets of non-primary waves at 368 and 372 degrees longitude that
 291 are propagating eastward. In Figures 4e, there is one, broader, region of non-primary waves
 292 spanning ~ 368 -371 degrees which propagate in both eastward and westward directions.
 293 The strong wind associated with the tide at 90 km altitude can act to critical level fil-
 294 ter waves propagating in the direction of the wind (or lead to significantly slower wave
 295 modes) and can cause reflection and evanescence of waves propagating against the wind
 296 (leading to rapidly decaying vertical aligned phase fronts). Either way, the amplitudes
 297 are diminished in this region as a result. Thus, the tidal wind acts as a filter, control-
 298 ling which non-primary waves can propagate from the breaking region to the thermo-
 299 sphere as noted previously by Becker and Vadas (2018). It is noted, however, that the
 300 wind is time invariant in these simulations and that hard critical levels and turning point
 301 levels become more transient when time dependence is included (e.g. Broutman & Young,
 302 1986; Eckermann, 1997; Heale & Snively, 2015; Senf & Achatz, 2011).

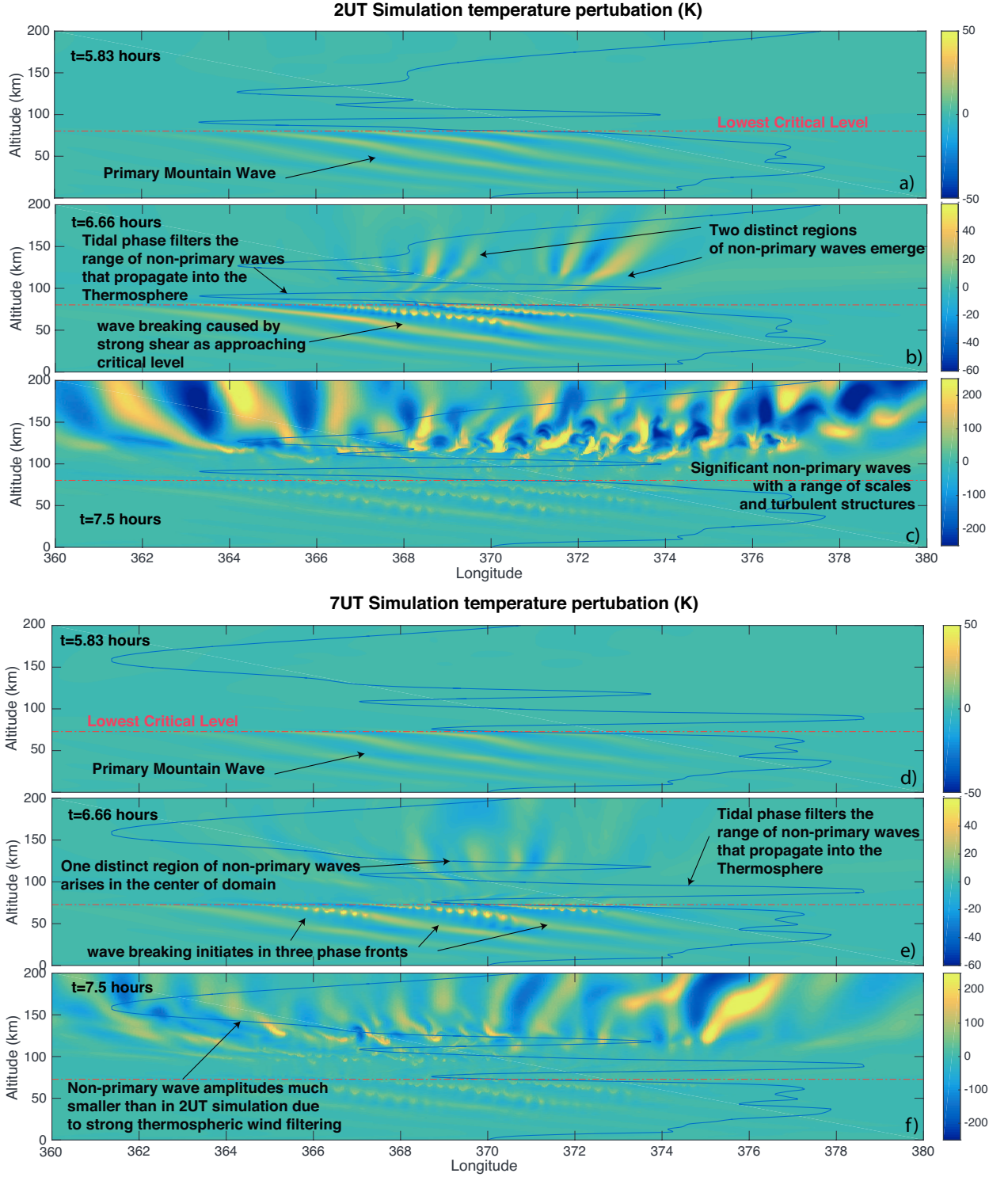


Figure 4. Temperature perturbation field at $t=5.83$, 6.6 , and 7.5 hours for the (a,b,c) 2 UT simulation and (d,e,f) 7 UT simulation. The horizontal red dotted line represents the lowest critical level the mountain wave encounters and the blue line represents the structure of the zonal wind.

At $t=7.5$ hours (Figures 4c and f), non-primary waves, at a range of scales, are dominant in the thermosphere (above 100 km) with amplitudes of up to 250 K. The initial non-primary waves, seen in Figures 4b and e, undergo further breaking and turbulence particularly at ~ 130 km altitude leading to further wave generation. Vadas and Becker (2019) show a similar scenario in their GCM simulations of mountain wave breaking over the Andes. They find that primary mountain waves breaking between 60-80km that generates secondary waves which are then dissipated around 110 km altitude, generate a further body force, and produce tertiary waves. However, the scales are very different in their study. In this study, we use the generic term non-primary to refer to any wave that is not the primary mountain wave so we do not have to keep count of the level of wave generation (secondary, tertiary etc). The differences in thermospheric wind in the 2 and 7 UT simulations cause noticeable differences in the non-primary wave dynamics in this region. In the 2 UT simulation (Figures 4c), waves propagate both eastward and westward, with the eastward propagating waves prone to breaking, while the westward propagating waves propagate more freely. In the 7 UT simulation (Figures 4f), westward propagating waves are severely filtered or damped by the strong westward wind, leaving the eastward propagating waves to possess the largest amplitudes. This shows the importance of understanding the nature of the thermospheric wind in determining the propagation and dissipation of non-primary waves in this region. Please see the supporting information for movies showing the evolution of the two wave fields.

5.3 Tidal filtering

Figure 5 shows a diagram of the horizontal wavelength and period combinations of AGWs that will be critical level filtered, evanescent, or freely propagating at 90 km altitude where the tidal wind is at its maximum amplitude. The primary mountain wave breaking occurs below this altitude and the non-primary waves are dominant above. The tidal wind then acts as a filter to allow certain modes to propagate from the mesosphere up into the thermosphere. For the 2 UT simulation, the tidal wind peaks at a westward amplitude of 65 m/s while it peaks at an eastward amplitude of 85 m/s for the 7 UT simulation. Thus, waves with horizontal phase speeds less than these respective winds will be critical level filtered (for waves propagating in the direction of the wind). For waves propagating against the wind, all wavelengths shorter than ~ 40 km are likely to be evanescent. It can be seen from Figure 5 that there are a broader range of waves that can freely

335 propagate against the tide than with it, and that a broader range of scales can propa-
 336 gate in the 2 UT case than the 7 UT case.

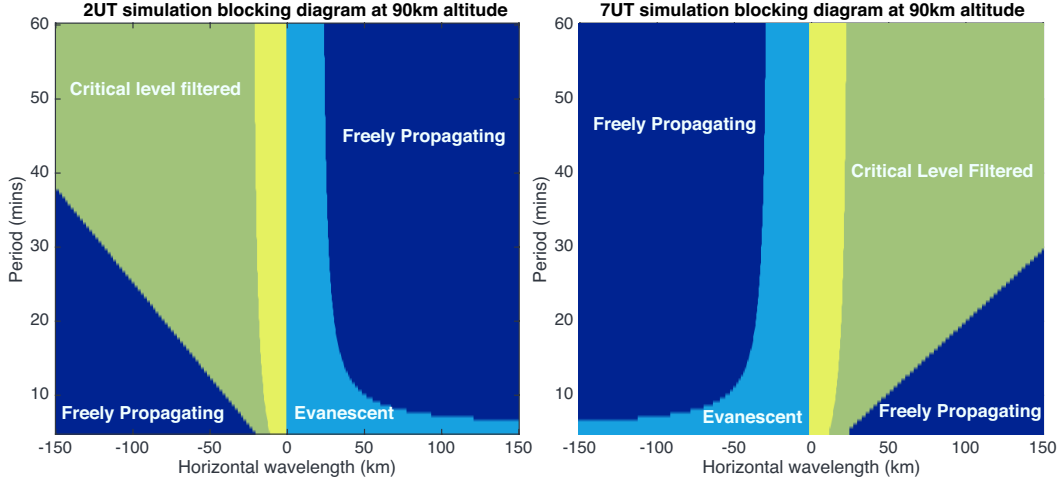


Figure 5. Blocking diagram showing the wavelength-period combinations for AGWs which are freely propagating, critical level filtered, or evanescent at 90km altitude where the tidal wind is strongest. The 2 UT simulation blocking diagram is shown on the left and the 7 UT on the right.

337 5.4 Association between initial wave breaking, wave forcing, and non- 338 primary waves

339 In this sub-section, we explore the connection between the breaking scales of the
 340 wave, the localized forcing created by momentum deposition associated with the break-
 341 ing, and the generation of non-primary waves. In particular, we look at the onset of break-
 342 ing and the initial non-primary waves that are created. In order to analyze the localized
 343 forcing, we calculate the horizontal and vertical forcing as defined in Zhou et al. (2002)
 344 and also used in Chun and Kim (2008).

$$F_u = -\frac{1}{\rho_0} \frac{\partial}{\partial x} (\rho_0 u'^2) - \left[-\frac{1}{\rho_0} \frac{\partial}{\partial z} (\rho_0 [u'w' - \overline{u'w'}]) \right] \quad (2)$$

$$F_w = -\frac{1}{\rho_0} \frac{\partial}{\partial x} (\rho_0 u'w') - \frac{1}{\rho_0} \frac{\partial}{\partial z} (\rho_0 [w'^2 - \overline{w'}]) \quad (3)$$

345 It is noted, however, that Chun and Kim (2008) states "these terms do not solely
 346 represent the momentum due to breaking of the primary waves. Rather, it represents

simply a nonlinear forcing for the linear gravity waves. The magnitude of the nonlinear forcing is directly related to the magnitude of the perturbations that represents waves, thus they are not completely separable.”

Figure 6 and 7 show the temperature perturbations at $t=6.58$ and 6.75 hours and the corresponding horizontal and vertical forcing at each of those times for the 2 UT and 7 UT simulations, respectively. A Morlet wavelet transform (Torrence & Compo, 1998) is used to examine the spatial spectrum of the temperature at $z=120\text{km}$ in panel a (representing the initial non-primary waves), and of the horizontal and vertical forcing from 60-80km altitude in panels d and h (the spectrum is averaged over this altitude and represents the primary wave breaking region).

Figure 6b and c shows that wave breaking occurs between 60-80 km altitude and is most visible within the warm fronts of the wave in the 2 UT simulation. The horizontal scales of the turbulent eddies in Figure 6b range from 8-15 km and occur along two of the mountain wave phase fronts. Non-primary waves can clearly be seen, just above the lowest red dotted line in panels b and c, emanating from the breaking region at those same eddy scales. However, non-primary waves at these scales cannot propagate above the tidal wind at 90 km altitude due to critical level filtering or reflection (depending upon the propagation direction). There are two distinct regions of non-primary waves that propagate (eastward) beyond the tidal winds at 90km into the thermosphere, which originate from each of the two breaking phase fronts (located at $x\sim 1350$ and 1550 km in Figure 6b and c). The most western packet of non-primary waves (at $x=1300-1400$ km in Figure 6b and c) have a dominant horizontal scale of 60 km at 120 km altitude (as labelled in Figure 6a) and are evanescent while propagating through the tidal wind field but tunnel through this region and can emerge above leading to both eastward and westward propagating waves. The eastern packet of non-primary waves ($x=1600-1700$ km in Figure 6b and c) have a broader range of horizontal scales from 50-180 km, with peak power at 90 km (also labelled Figure 6a).

The second row of Figure 6 shows the horizontal forcing (F_u , panels e, and f) and its wavelet spectrum averaged over 60-80km altitude (panel d). Three dominant horizontal forcing scales arise at 15, 110, and 215km in panel d. The 15km horizontal forcing in Figure 6d corresponds to the prominent eddy scales seen in Figure 6b and c, and produce non-primary waves that are filtered by the tide. The 110km forcing in Figure

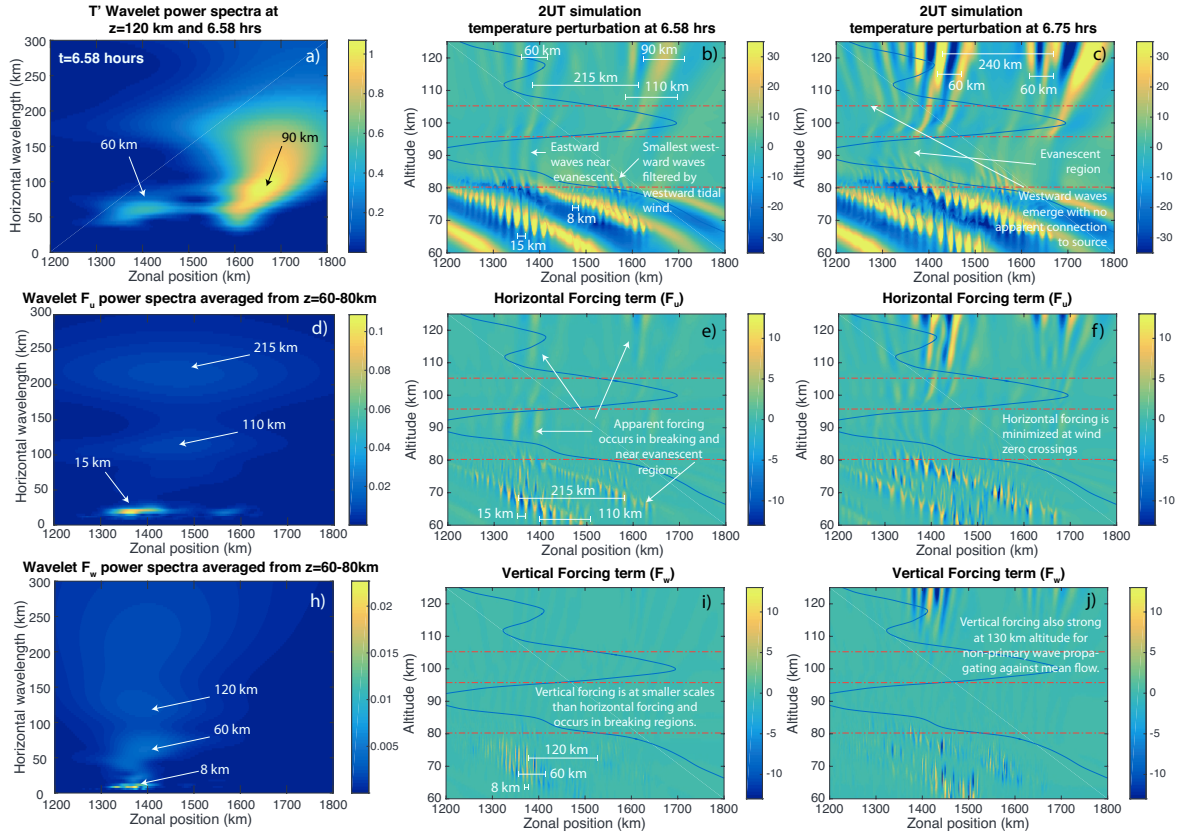


Figure 6. The temperature perturbation (K) (b,c), horizontal forcing term ($F_u(m/s^2)$) (e,f), and vertical forcing term ($F_w(m/s^2)$) (i,j) at $t=6.58$ and 6.75 hours for the 2 UT simulation. The left hand panel shows a wavelet transform of (a) the temperature at $z=120$ km, highlighting the propagating non-primary wave scales, (d) the horizontal forcing scales averaged from 60-80km, and (h) the vertical forcing scales averaged from 60-80km.

6d corresponds to the horizontal width of one of the breaking phase fronts (labelled in panel e), while the 215km scale, in Figure 6d, corresponds to the distance between the two breaking mountain wave phase fronts (also labelled in panel e). Weak horizontal forcing is also present in the westward winds in the thermosphere (for eastward propagating waves), due to evanescent decay of the wave and due to nonlinear forcing in the regions above 110 km altitude. It is noted that the apparent forcing in the evanescent is not a body forcing as would occur for wave dissipation by viscosity/conduction or a forcing as produced by breaking. Rather, the apparent vertical momentum flux divergence is associated with the exponential decay which occurs in an evanescent region. The 110km scale forcing, in Figure 6e, leads to the approximate packet scale of each of the two non-primary wave regions in panel b and the 215km scale produces the spacing between these two non-primary wave regions.

The third row of Figure 6 shows the vertical forcing (F_w , panels i and j) and its wavelet spectrum averaged over 60-80km altitude (panel h). The dominant scale of this forcing labelled in panel i, at 8 km, is much smaller than the horizontal forcing in panel e. This 8 km scale forcing clearly couples to non-primary gravity waves (Figure 6b at $x=1550\text{km}$, $z=80\text{ km}$), however these waves cannot propagate above the strong tidal wind at 90km altitude. The wavelet spectra (panel h) also shows power at 40-90 km (peaking at 60km), 120km, and 240km horizontal scales. The 40-90 km horizontal scale arises from the widths of the vertical forcing within one breaking mountain wave front and the larger scales arise from the forcing associated with the breaking between two mountain wave phase fronts (labelled in panel i). The 60-90km horizontal scales of vertical forcing in panel i correspond to the dominant non-primary waves seen propagating at 120km altitude in panel b and c. The evidence in this figure, while showing correlation rather than causation, suggests that the horizontal forcing contributes to packet scales of the non-primary waves, while the vertical forcing helps govern the horizontal wavelength of the propagating waves shortly after the onset of breaking.

Figure 7a shows significant non-primary wave power at horizontal scales between 60-120km. These scales are similar to those observed in the Figure 6a, however, the non-primary wave regions are not as distinct and propagate in both eastward and westward directions. As mentioned previously, three phase fronts can be seen breaking in panel b of the 7 UT case as opposed to two in panel b of the 2 UT case. As with the 2 UT case,

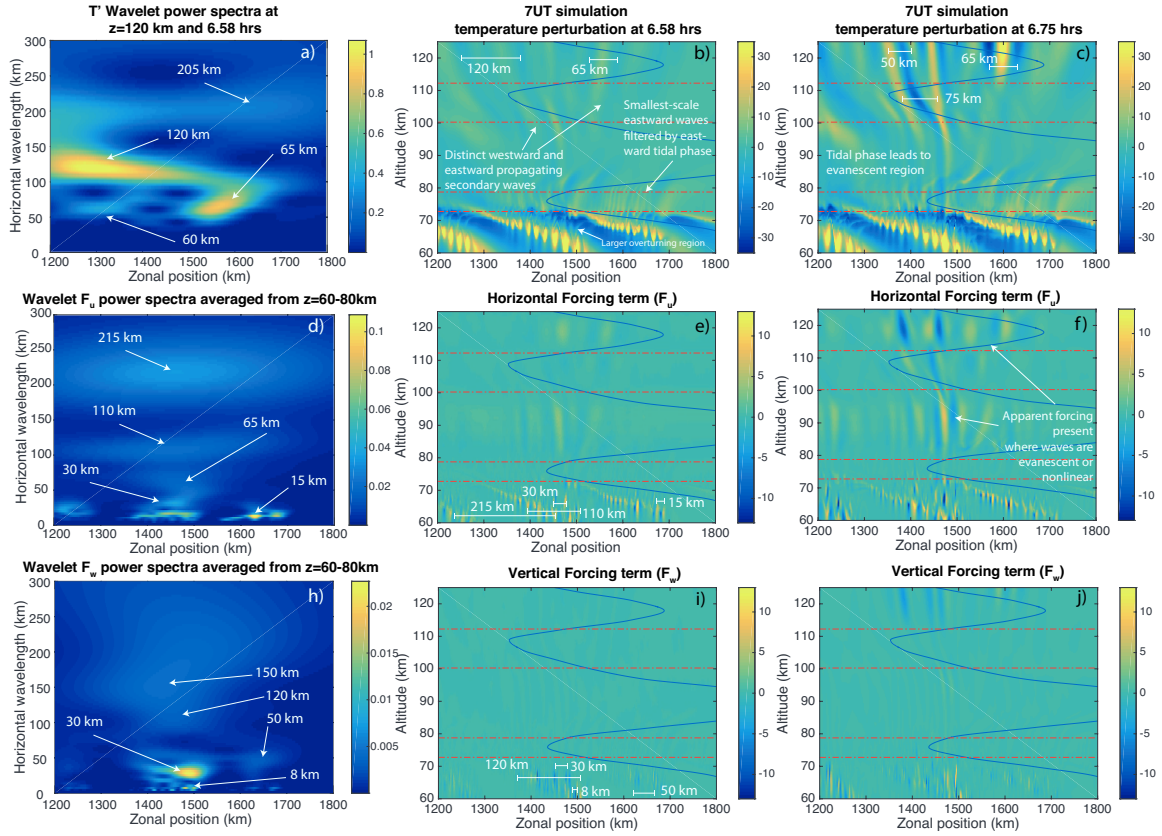


Figure 7. The temperature perturbation (K) (b,c), horizontal forcing term ($F_u(m/s^2)$) (e,f), and vertical forcing term ($F_w(m/s^2)$) (i,j) at $t=6.58$ and 6.75 hours for the 7 UT simulation. The left hand panel shows a wavelet transform of (a) the temperature at $z=120$ km, highlighting the propagating non-primary wave scales, (d) the horizontal forcing scales averaged from 60-80 km, and (h) the vertical forcing scales averaged from 60-80 km.

the smallest scales of breaking generate waves which are filtered or reflected by the tidal wind.

In the second row of Figure 7 (horizontal forcing), notable scales of horizontal forcing are seen at 15km, 30km, 65km, 110km, and 215km in panel d. The 15, 110, and 215km modes are the same as those seen in the 2 UT case and are defined by the breaking scales, mountain wave phase front scale, and mountain wave horizontal scale respectively. However, the 30-65km scales in panel d are not present in the 2 UT simulation and appear to arise from a larger overturning region formed between two vertical phases of the wave in the middle of the domain (labelled in panel b). The 60-65km scale transfers into non-primary propagating waves which are dominant at 120km altitude in panels b and c, while the 30km mode is filtered.

Figure 7h (vertical forcing) displays prominent scales of 8 and 30km with a weaker mode at 50-60km and a continuum of scales from 100-250km (with relative peaks at 120 and 150km). The 8 and 30km modes are filtered or evanescent over the region dominated by the tidal wind at 90km altitude. The larger scale modes, particularly at 60 and 120km, appear to couple efficiently in to propagating non-primary waves (seen at $z=120$ km in panel c) at these early onset breaking stages and are defined by the widths of vertical forcing within one breaking mountain wave phase front.

Since Figure 6 and 7 show the early stages of breaking, and most phase lines can be traced to the source region, it is suggested that most of the waves seen here are non-primary waves connected to the initial mountain wave breaking. However, some waves emerge above 100km altitude, with both westward and eastward propagation directions, that have no direct phase lines connected to the source region. The presence of evanescence and tunneling in both the 2UT and 7UT cases complicates the connection between the waves generated by the breaking of the mountain wave and the propagating non-primary waves in the upper thermosphere. The westward and eastward waves could simply be the emergence of ‘waves’ that tunnel through the evanescent region and continue to propagate according to the local wind and shear as they emerge. However, it could also be the case that some of the waves are generated by further wave dissipation as described by Vadas and Becker (2019). In this mechanism, initial non-primary waves are further dissipated or break (between 80-130 km, peaking at 110 km in their study) which generates body forces that produce further waves. This mechanism can continue multiple

times producing additional non primary waves. It is certainly the case that the further breaking of non-primary waves occurs at later times, as seen in Figure 4 c and f between 100-150 km altitude. It is unclear how much this mechanism contributes to the propagating non-primary waves versus those that tunnel through the evanescent layer or from direct propagation.

5.5 Non-primary wave spectra

In the previous subsection, the breaking scales, resulting forces, and coupling to the initial non-primary wave scales was examined. In this subsection, the periods and scales of the waves are examined over the entire duration and domain of the simulation. As such, these spectra contain the mountain wave, and all non-primary. Figure 8 shows the Fourier transform of the temperature perturbation at 60-80 (averaged), 100, 130, and 150km altitude for both the 2 UT and 7 UT simulations.

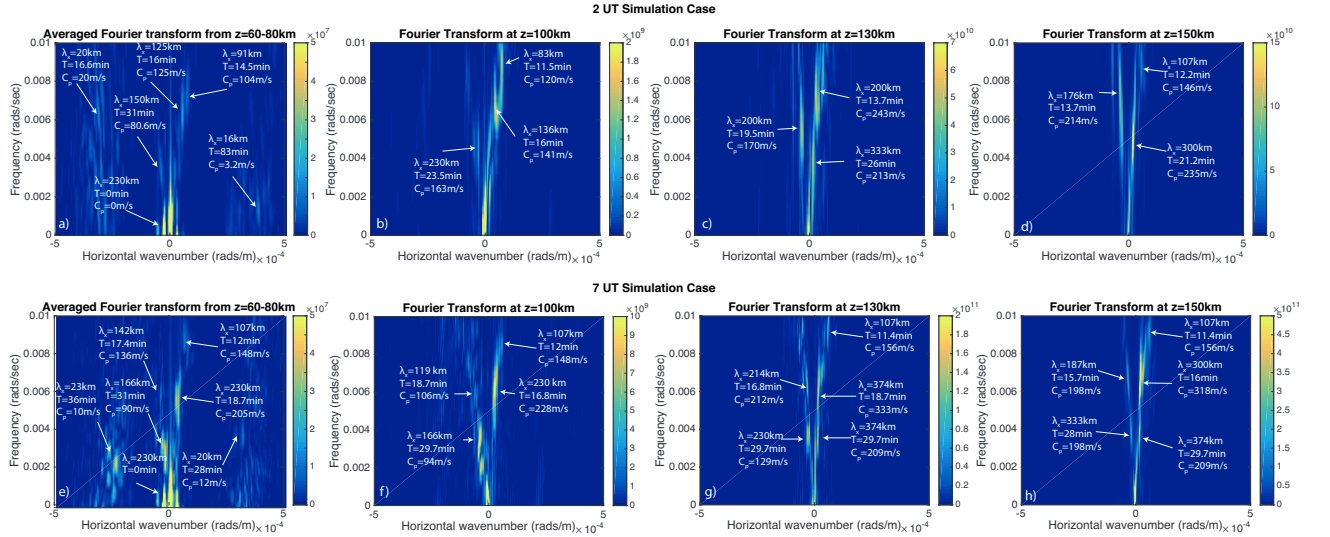


Figure 8. Fourier transform of the temperature perturbation for (a-d) the 2 UT simulation and (e-i) the 7 UT simulation at 60-80 (averaged), 100, 130, and 150 km altitude.

Figure 8a and e show the scales and periods of the waves associated with the primary mountain wave and those generated by its breaking and nonlinearity. With the exception of power at the zeroth order, the strongest mode is the mountain wave (230 km, 0 period). The small-scale breaking scales (8-30 km) that are seen below the first red dotted line in Figures 6b and 7b are present in the spectra in Figure 8a and e, but are not

particularly strong relative to the mountain wave. Waves generated at these scales and periods have very slow phase speeds (~ 10 s m/s) which is why they are easily filtered out by the tidal winds and do not appear in the spectra at 100, 130, or 150km altitude.

In the 2UT simulation, three distinct regions of wave power are observed over the 60-80km altitude region, in Figure 8a, which are centered at 150km and 31 mins (propagating westward), 125 km and 16 mins, and 91 km and 14.5 mins (propagating eastward). At 100km altitude, in Figure 8b (above the strong tidal wind phase), there are still three distinct modal regions but the central wavelength and periods change to 230km and 23.5 mins (westward propagating), 136km and 16 mins, and 83km and 11.5 mins (eastward propagating) respectively. The 136km and 16 min period dominant mode seen in Figure 8b can be correlated to a corresponding mode in Figure 8a, at $z=60-80$ km (centered at 125km and 16 mins), but it is difficult to draw any strong conclusions between the relationship of the other regions other than they share similar periods. The central wavelength and periods change again at both 130km and 150km, in Figure 8c and d respectively, but the following general trends are true: The eastward mode has the strongest spectral amplitude, there are two distinct modal regions eastward and one westward, the spectra becomes more bandwidth limited in wavelength, but more diffuse in period, as the altitude increases. This occurs because the increasing viscosity with altitude preferentially damps smaller scales and “smooths” wave modes to remove discrete turbulent-like features. The phase speeds in the thermosphere are in the 150-250 m/s range.

In the 7 UT simulation case, over the 60-80km altitude region (Figure 8e), there is one dominant westward propagating mode (166km and 31 mins) and one dominant eastward propagating mode (230km, 18.7 mins) with two weaker modes present as well (142km, 17.4 mins, westward and 107km, 12 mins eastward). Unlike in the 2 UT case, the spectral periods at $z=100$ km (Figure 8f), 130 (Figure 8g), and 150km (Figure 8h) corresponds fairly well to the spectral periods over 60-80km (Figure 8e). A strong case could be made that the non-primary wave modes seen in the thermosphere are a direct result of the modes arising from the breaking and nonlinearity of the mountain wave in the mesosphere.

However, the situation is complicated by the fact that there is more than one level of breaking as can be seen in Figure 4c and f. Therefore, waves in the upper atmosphere could be generated by multiple levels of breaking and new wave production (Vadas &

Becker, 2019). It is difficult to trace the origins of spectral components in the thermosphere directly to regions in the primary wave vicinity. In addition, the strongest wave modes at $z=150\text{km}$ have a horizontal scale larger than the primary wave (300km) in both the 2 UT and 7 UT simulations. Theory suggests that wave breaking produces scales and periods that are smaller and faster than the primary wave mode (Y.-H. Kim & Chun, 2008), while packet scale dissipation (for a single packet) creates body forces that produce waves that are larger scale and longer period than the primary wave (Vadas et al., 2018). The latter mechanism is better suited to explaining the large wave scales dominant at 150km altitude, however the periods are 16 and 22 minutes respectively, which are much much shorter than the quasi-stationary primary mountain wave. Vadas and Becker (2019) found that the dissipation of intersecting wave packets can lead to constructive and destructive forcing that generates waves with horizontal wavelengths smaller than the initial packet. It is also noted that very localized forcings (in either space or time) can produce a broad spectra of waves (Heale et al., 2014, 2018), a prominent example of which are convective forcings from individual thunderstorm plumes (Alexander & Holton, 2004; Beres, 2004; Lane, Reeder, & Clark, 2001). Therefore, localized forcings, such as those that arise from the small breaking scales or constructive/destructive interference of several wave packets, could credibly produce a broad spectra of waves with high temporal variability. This result was also found in Vadas and Crowley (2010) and could explain the relatively short periods of the large scale waves at $z=150\text{ km}$.

5.6 Spatial distribution of wave forcing

In this subsection, the time-averaged forcing magnitude is analyzed for both the 2 UT and 7 UT cases. The quantity analyzed is $F_t = \sqrt{\overline{F_u^2} + \overline{F_w^2}}$, where the over-line represents the time-average over the entire simulation. The time averaged forcing magnitudes are presented in Figure 9. The first thing to note is that there is a huge difference between the distribution of wave forcing in the thermosphere in the 2 UT and 7 UT simulations. Secondly, the strongest forcing arises from non primary waves that are currently not accounted for in General Circulation Models (GCMs). This suggests that wave forcing in the MLT and thermosphere are likely significantly underestimated in these models over mountains (Vadas et al., 2019).

In the 2 UT simulation (Figure 9a), the wave forcing is distributed over a fairly broad area in the thermosphere, ranging from 360-380 degrees longitude and 100-220km alti-

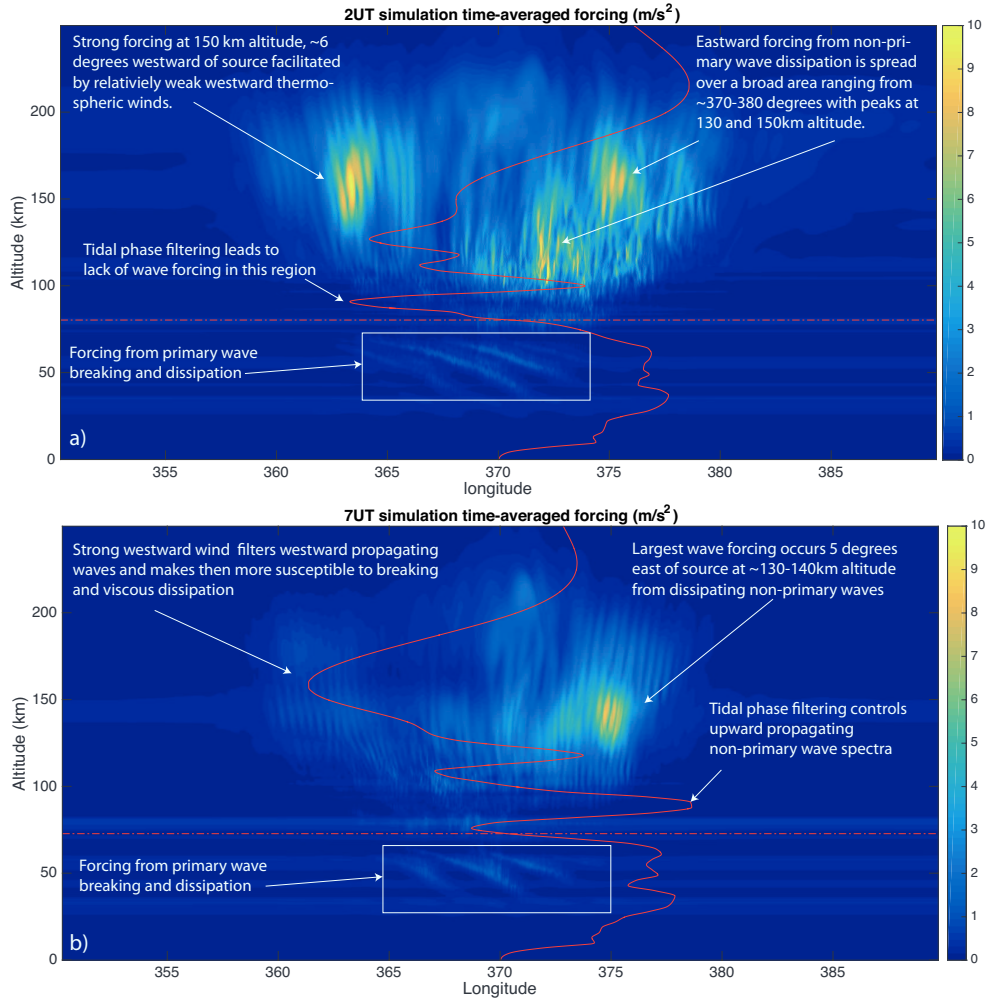


Figure 9. The time-averaged magnitude of the wave forcing for the a) 2 UT and the b) 7 UT simulation.

tude. There are three distinct regions of strong forcing, one is westward of the source
 and peaks at 150km altitude and 363 degrees longitude, the other two are eastward of
 the source with peaks at 130 and 150km altitude and 372 and 375 degrees longitude re-
 spectively. In comparison, the 7 UT simulation (Figure 9b) only displays a region of strong
 forcing eastward of the source at 150km and 375 degrees longitude. This difference can
 be attributed to the differences in the thermospheric wind in both simulations. The strong
 westward thermospheric wind (which peaks at $\sim 90\text{m/s}$ at 160km altitude) in Figure 9b
 acts to filter and refract westward propagating waves to smaller vertical scales which in-
 creases the rate at which they are dissipated. Therefore, the westward propagating waves
 that are present in the 2 UT simulation are removed by filtering and dissipation in the
 7 UT simulation. This effect is clearly visible in Figure 4f, the westward non-primary
 waves are breaking at $\sim 130\text{km}$ altitude where the westward zonal shear is maximized
 and are reduced to small scales which are readily dissipated. The eastward waves have
 much larger vertical scale, can propagate to higher altitudes and as such obtain larger
 amplitudes before dissipating. In contrast, the eastward waves in Figure 4c are break-
 ing and have smaller vertical scales than the westward waves due to the wind shear be-
 ing eastward above $\sim 130\text{km}$ altitude. The differences in the eastward forcing in the 2
 UT and 7 UT simulations can be attributed to the tidal wind phase at 90km altitude
 acting to filter the range of non-primary waves that can propagate up into the thermo-
 sphere. The phase of the 2 UT simulation tide is westward and of smaller magnitude than
 in the 7 UT simulation. As such, a greater range of eastward propagating non-primary
 waves can propagate from the mountain wave breaking region up into the thermosphere
 in the 2 UT simulation than in the 7 UT simulation where they are filtered by the strong
 eastward tide.

Figure 9 shows the importance of the tidal phase and thermospheric wind dynam-
 ics in governing the wave forcing due to non-primary waves in the thermosphere. While
 the primary mountain wave also produces a wave forcing in both simulations, the time
 averaged amplitude is half that of the peak forcing due to non-primary waves in the ther-
 mosphere.

6 Summary and conclusions

In this study, we simulated a strong, persistent mountain wave observed over north-
 ern Europe on the 12th January 2016 using the MAGIC model in 2D. Two simulations

were run with fixed background zonal wind structure taken at 2 and 7 UT respectively and representing opposing tidal phases. The aim of the study was to investigate the nature of the mountain wave breaking, dissipation, and non-primary wave generation in the mesosphere and thermosphere with different background wind conditions. The simulations showed breaking of the mountain wave as it approaches a critical level in the mesosphere which generated a broad range of non-primary waves which propagated both eastward and westward. The dominant turbulent horizontal scales produced by the breaking mountain wave were between 8-30 km, with larger forcing scales defined by the approximate width of the each phase of the mountain wave (~ 110 - 150 km) and the spacing between horizontal phases (~ 215 - 250 km). The dominant turbulent scales couple directly to horizontal scales of propagating non-primary waves, however, these waves are critical level filtered (or rendered evanescent, depending upon direction of propagation) by the strong tidal wind at 90 km altitude and do not propagate up into the thermosphere. The tidal phase and amplitude acts like a filter and controls the spectra of non-primary waves that can propagate up into the thermosphere. It is noted, however, that if the background winds were time dependent, the amount of critical level filtering and evanescence would likely be reduced. This will be investigated in future studies. The initial non-primary waves that propagate up into the thermosphere (above 100 km) have horizontal scales between 60-120 km with the wave scales influenced by both the horizontal and vertical forcing scales. Over the course of the simulation, the non-primary waves that are most dominant at 150 km altitude have distinct scales at 107 km, 170-190 km, and 300 km with periods of 11-12 mins, 14-16 mins, and 16-22 mins respectively. The phase speeds range from 140-318 m/s. It is also noted that the term non-primary wave is more appropriate than non-primary wave, since the waves break more than once generating a cascade of scales and periods. The time averaged wave forcing magnitude resulting from non-primary wave dissipation and nonlinearity in thermosphere is significant ($\sim 2\times$ the forcing from the dissipating primary wave) and peaks between 130-150 km altitude. The spatial distribution of wave forcing is heavily influenced by the thermospheric winds. In the 2 UT simulation, wave forcing is strong both eastward and westward of the source and the distribution is broadly spaced as a result of the weaker thermospheric winds between 100-150 km altitude. In the 7 UT simulation, strong westward winds and shears lead to filtering, breaking and dissipation of the westward propagating wind leaving a relatively localized region of strong forcing eastward of the source. Understanding the thermospheric

wind dynamics will be crucial to determining the forcing generated by non-primary waves in the upper atmosphere. Non-primary waves can contribute significantly to the wave forcing of the upper atmosphere and are currently unaccounted for in the GCM parameterizations. While beyond the scope of this paper, downward propagating non-primary waves can also reduce the momentum flux in the mesosphere and stratosphere (Chun & Kim, 2008). Taking these processes into account will be crucial to producing more realistic atmospheric forcing predictions from gravity waves in both the middle and upper atmosphere. Further studies will include the time-dependence of the tides and extend these studies to 3D.

Acknowledgments

Research by Christopher Heale was carried out under NSF grant AGS-1822551, Katrina Bossert was supported under NSF grant AGS-1822585, and Sharon Vadas was supported by NSF Grant AGS-1822867. We thank the editor and reviewers for their time and effort in improving this manuscript. Simulation data will be made available at <https://commons.erau.edu/dm-secondary-gravity-waves-europe/>. AIRS data is publicly available at https://airs.jpl.nasa.gov/data/get_data and ECMWF reanalysis datasets are available at <https://apps.ecmwf.int/datasets/>. Access to the ECMWF data was possible through the special project “Deep vertical propagation of internal gravity waves by AD. Part of this research was conducted within the scope of the German research initiative Role of the middle atmosphere in climate (ROMIC) under grant 01LG1206A provided by the Germany ministry for Education and Research. Partial funding was also provided by the German Science foundation (DFG) via the research unit MSGWaves (GW-TP/DO 1020/9-1, PACOG/RA 1400/6-1).

References

- Achatz, U. (2007). Gravity-wave breaking: Linear and primary nonlinear dynamics. *Adv. Space Res.*, *40*, 719-733.
- Alexander, M. J., & Holton, J. R. (1997). A Model Study of zonal Forcing in the Equatorial Stratosphere by Convectively Induced Gravity Waves. *J. Atmos. Sci.*, *54* (doi:10.1175/1520-0469(1997)054<0408:AMSOZF;2.0.CO;2>), 408-419.
- Alexander, M. J., & Holton, J. R. (2004). On the spectrum of vertically propagating gravity waves generated by a transient heat source. *Atmos. Chem. Phys.*, *4* (doi:10.5194/acp-4-923-2004), 923-932.

- 620 Alexander, M. J., & Rosenlof, K. H. (1996). Nonstationary gravity wave forcing
621 of the stratospheric zonal mean wind. *J. Geophys. Res. Atmos.*, 101(D18),
622 23465–23474. Retrieved from <http://dx.doi.org/10.1029/96JD02197> doi:
623 10.1029/96JD02197
- 624 Alexander, M. J., & Rosenlof, K. H. (2003). Gravity-wave forcing in the strato-
625 sphere: Observational constraints from the upper atmosphere research satellite
626 and implications for parameterization in global models. *J. Geophys. Res. At-
627 mos.*, 108(D19). Retrieved from [https://agupubs.onlinelibrary.wiley](https://agupubs.onlinelibrary.wiley.com/doi/abs/10.1029/2003JD003373)
628 [.com/doi/abs/10.1029/2003JD003373](https://agupubs.onlinelibrary.wiley.com/doi/abs/10.1029/2003JD003373) doi: 10.1029/2003JD003373
- 629 Andreassen, Ø., Wasberg, C.-E., Fritts, D. C., & Isler, J. R. (1994). Gravity wave
630 breaking in two and three dimensions, 1, Model description and comparison of
631 two-dimensional evolutions. *J. Geophys. Res.*, 99, 8095-8108.
- 632 Aumann, H. H., Chahine, M. T., Gautier, C., Goldberg, M. D., Kalnay, E.,
633 McMillin, L. M., ... Susskind, J. (2003, doi:10.1109/TGRS.2002.808356).
634 AIRS/AMSU/HSB on the aqua mission: design, science objectives, data prod-
635 ucts, and processing systems. *IEEE Transactions on Geoscience and Remote*
636 *Sensing*, 41(2), 253-264.
- 637 Bacmeister, J. T. (1993). Mountain-wave drag in the stratosphere and meso-
638 sphere inferred from observed winds and a simple mountain-wave param-
639 eterization scheme. *J. Atmos. Sci.*, 50(3), 377-399. Retrieved from
640 [https://doi.org/10.1175/1520-0469\(1993\)050<0377:MWDITS>2.0.CO;2](https://doi.org/10.1175/1520-0469(1993)050<0377:MWDITS>2.0.CO;2)
641 doi: 10.1175/1520-0469(1993)050<0377:MWDITS>2.0.CO;2
- 642 Bacmeister, J. T., & Schoeberl, M. R. (1989). Breakdown of vertically propagating
643 two-dimensional gravity waves forced by orography. *J. Atmos. Sci.*, 46(14),
644 2109-2134. Retrieved from [https://doi.org/10.1175/1520-0469\(1989\)](https://doi.org/10.1175/1520-0469(1989)046<2109:BOVPTD>2.0.CO;2)
645 [046<2109:BOVPTD>2.0.CO;2](https://doi.org/10.1175/1520-0469(1989)046<2109:BOVPTD>2.0.CO;2) doi: 10.1175/1520-0469(1989)046(2109:
646 BOVPTD)2.0.CO;2
- 647 Baldwin, M. P., Gray, L. J., Dunkerton, T. J., Hamilton, K., Haynes, P. H., Randel,
648 W. J., ... Takahashi, M. (2001). The quasi-biennial oscillation. *Rev. Geophys.*,
649 39(2), 179–229. Retrieved from <http://dx.doi.org/10.1029/1999RG000073>
650 doi: 10.1029/1999RG000073
- 651 Bale, D. S., LeVeque, R. J., Mitran, S., & Rossmanith, J. A. (2002). A wave prop-
652 agation method for conservation laws and balance laws with spatially varying

- flux functions. *J. Sci. Comput.*, *24*(3), 955-978.
- Becker, E., & Vadas, S. L. (2018). Secondary gravity waves in the winter mesosphere: Results from a high-resolution global circulation model. *J. Geophys. Res. Atmos.*, *123*(5), 2605-2627. Retrieved from <https://agupubs.onlinelibrary.wiley.com/doi/abs/10.1002/2017JD027460> doi: 10.1002/2017JD027460
- Beres, J. H. (2004, doi:10.1175/1520-0469(2004)061). Gravity wave generation by a three-dimensional thermal forcing. *J. Atmos. Sci.*, *61*, 1805-1815.
- Booker, J. R., & Bretherton, F. P. (1967). The critical layer for internal gravity waves in a shear flow. *J. Fluid Mech.*, *27*, 513-539.
- Bossert, K., Fritts, D., Pautet, P.-D., Williams, B. P., Taylor, M. J., Kaifler, B., ... MacKinnon, A. D. (2015). Momentum flux estimates accompanying multiscale gravity waves over Mount Cook, New Zealand, on 13 July 2014 during the DEEPWAVE campaign. *J. Geophys. Res. Atmos.*, *120*(doi:10.1002/2015JD023197).
- Bossert, K., Kruse, C. G., Heale, C. J., Fritts, D. C., Williams, B. P., Snively, J. B., ... Taylor, M. J. (2017). Secondary gravity wave generation over new zealand during the deepwave campaign. *J. Geophys. Res. Atmos.*, *122*(15), 7834-7850. Retrieved from <https://agupubs.onlinelibrary.wiley.com/doi/abs/10.1002/2016JD026079> doi: 10.1002/2016JD026079
- Bramberger, M., Dörnbrack, A., Bossert, K., Ehard, B., Fritts, D. C., Kaifler, B., ... Witschas, B. (2017). Does strong tropospheric forcing cause large-amplitude mesospheric gravity waves? a deepwave case study. *J. Geophys. Res. Atmos.*, *122*(21), 11,422-11,443. Retrieved from <https://agupubs.onlinelibrary.wiley.com/doi/abs/10.1002/2017JD027371> doi: 10.1002/2017JD027371
- Broutman, D., & Young, W. (1986). On the interaction of small-scale oceanic internal waves with near-inertial waves. *J. Fluid. Mech.*, *166*, 341-358.
- Chun, H.-Y., & Kim, Y.-H. (2008). Secondary waves generated by breaking of convective gravity waves in the mesosphere and their influence in the wave momentum flux. *J. Geophys. Res. Atmos.*, *113*(D23). Retrieved from <https://agupubs.onlinelibrary.wiley.com/doi/abs/10.1029/2008JD009792> doi: 10.1029/2008JD009792

- Dörnbrack, A. (1998). Turbulent mixing by breaking gravity waves. *J. Fluid. Mech.*, 375(doi:10.1017/S0022112098002833), 113-141.
- Dörnbrack, A., Gisinger, S., Pitts, M. C., Poole, L. R., & Maturilli, M. (2017, doi:10.1175/MWR-D-16-0214.1). Multilevel cloud structures over svalbard. *Mon. Wea. Rev.*, 145(4), 1149-1159.
- Dörnbrack, A., Leutbecher, M., Kivi, R., & Kyro, E. (1999). Mountain-wave induced record low stratospheric temperatures above northern Scandinavia. *Tellus, Ser. A*, 51, 951-963.
- Drob, D. P., Emmert, J. T., Crowley, G., Picone, J. M., Shepherd, G. G., Skinner, W., ... Vincent, R. A. (2008). An empirical model of the earth's horizontal wind fields: HWM07. *J. Geophys. Res.*, 113(A12304), doi:10.1029/2008JA013668.
- Dunkerton, T. J. (1997). The role of gravity waves in the quasi-biennial oscillation. *Journal of Geophysical Research: Atmospheres*, 102(D22), 26053-26076. Retrieved from <https://agupubs.onlinelibrary.wiley.com/doi/abs/10.1029/96JD02999> doi: 10.1029/96JD02999
- Durran, D., & Klemp, J. (1987, [https://doi.org/10.1175/1520-0469\(1987\)044<3402:ALADWP;2.0.CO;2](https://doi.org/10.1175/1520-0469(1987)044<3402:ALADWP;2.0.CO;2)). Another look at downslope winds. part ii: Nonlinear amplification beneath wave-overturning layers. *J. Atmos. Sci.*, 44, 3402-3412.
- Eckermann, S. D. (1997). Influence of Wave Propagation on the Doppler Spreading of Atmospheric Gravity Waves. *J. Atmos. Sci.*, 54.
- Eckermann, S. D., Broutman, D., Ma, J., Doyle, J. D., Pautet, P.-D., Taylor, M. J., ... Smith, R. B. (2016). Dynamics of orographic gravity waves observed in the mesosphere over the auckland islands during the deep propagating gravity wave experiment (deepwave). *J. Atmos. Sci.*, 73(10), 3855-3876. Retrieved from <https://doi.org/10.1175/JAS-D-16-0059.1> doi: 10.1175/JAS-D-16-0059.1
- Ehard, B., Achtert, P., Dörnbrack, A., Gisinger, S., Gumbel, J., Khaplanov, M., ... Wagner, J. (2016). Combination of lidar and model data for studying deep gravity wave propagation. *Mon. Wea. Rev.*, 144(1), 77-98. Retrieved from <https://doi.org/10.1175/MWR-D-14-00405.1> doi: 10.1175/MWR-D-14-00405.1

- Ehard, B., Kaifler, B., Dörnbrack, A., Preusse, P., Eckermann, S. D., Bramberger, M., ... Rapp, M. (2017, doi:10.1002/2016JD025621). Horizontal propagation of large-amplitude mountain waves into the polar night jet. *J. Geophys. Res. Atmos.*, *122*(3), 1423-1436.
- Ehard, B., Malardel, S., Dörnbrack, A., Kaifler, B., N., Kaifler, & Wedi, N. (2018, doi: 10.1002/qj.3206). Comparing ECMWF high-resolution analyses with lidar temperature measurements in the middle atmosphere. *Quarterly Journal of the Royal Meteorological Society*, *144*(712), 633-640.
- Ern, M., Ploeger, F., Preusse, P., Gille, J. C., Gray, L. J., Kalisch, S., ... Riese, M. (2014). Interaction of gravity waves with the qbo: A satellite perspective. *Journal of Geophysical Research: Atmospheres*, *119*(5), 2329-2355. Retrieved from <https://agupubs.onlinelibrary.wiley.com/doi/abs/10.1002/2013JD020731> doi: 10.1002/2013JD020731
- Franke, P., & Robinson, W. (1999). Nonlinear behavior in the propagation of atmospheric gravity waves. *J. Atmos. Sci.*, *56*, 3010-3027.
- Fritts, D. C., & Alexander, M. J. (2003). Gravity wave dynamics and effects in the middle atmosphere. *Rev. Geophysics*, *41*(1).
- Fritts, D. C., Smith, R. B., Taylor, M. J., Doyle, J. D., Eckermann, S. D., Dornbrack, A., ... Ma, J. (2015). The Deep Propagating Gravity Wave Experiment (DEEPWAVE): An Airborne and Ground-Based Exploration of Gravity Wave Propagation and Effects from their Sources throughout the Lower and Middle Atmosphere. *Am. Met. Soc.*, <http://dx.doi.org/10.1175/BAMS-D-14-00269.1>. Retrieved from <https://www.eol.ucar.edu/node/5779>
- Fritts, D. C., Vosper, S. B., Williams, B. P., Bossert, K., Plane, J. M. C., Taylor, M. J., ... Murphy, D. J. (2018). Large-amplitude mountain waves in the mesosphere accompanying weak cross-mountain flow during deepwave research flight rf22. *J. Geophys. Res. Atmos.*, *123*(18), 9992-10,022. Retrieved from <https://agupubs.onlinelibrary.wiley.com/doi/abs/10.1029/2017JD028250> doi: 10.1029/2017JD028250
- Fritts, D. C., Wang, L., Werne, J., Lund, T., & Wan, K. (2009). Gravity wave instability and dynamics at high Reynolds numbers. Part i: Wave field evolution at large amplitudes and high frequencies. *J. Atmos. Sci.*, *66*, 1126-1147.
- Garcia, R. R., & Solomon, S. (1985). The effect of breaking gravity waves on the dy-

- namics and chemical composition of the mesosphere and lower thermosphere.
J. Geophys. Res., *90*, 3850-3868.
- Heale, C. J., Bossert, K., Snively, J. B., Fritts, D. C., Pautet, P.-D., & Taylor,
 M. J. (2017). Numerical modeling of a multiscale gravity wave event
 and its airglow signatures over mount cook, new zealand, during the deep-
 wave campaign. *J. Geophys. Res. Atmos.*, *122*(2), 846–860. Retrieved
 from <http://dx.doi.org/10.1002/2016JD025700> (2016JD025700) doi:
 10.1002/2016JD025700
- Heale, C. J., & Snively, J. B. (2015). Gravity wave propagation through a vertically
 and horizontally inhomogeneous background wind. *J. Geophys. Res.*, *120*(doi:
 10.1002/2015JD023505), 5931-5950.
- Heale, C. J., Snively, J. B., Hickey, M. P., & Ali, C. J. (2014). Thermospheric
 dissipation of upward propagating gravity wave packets. *J. Geophys. Res.*,
119(doi:10.1002/2013JA019387), 3857-3872.
- Heale, C. J., Walterscheid, R. L., & Snively, J. B. (2018). Localization effects on
 the dissipation of gravity wave packets in the upper mesosphere and lower
 thermosphere. *J. Geophys. Res. Atmos.*, *0*(0). Retrieved from [https://](https://agupubs.onlinelibrary.wiley.com/doi/abs/10.1029/2017JD027617)
agupubs.onlinelibrary.wiley.com/doi/abs/10.1029/2017JD027617 doi:
 10.1029/2017JD027617
- Hickey, M. P., Walterscheid, R. L., & Schubert, G. (2011). Gravity wave heating and
 cooling of the thermosphere: Roles of the sensible heat flux and viscous flux of
 kinetic energy. *J. Geophys. Res.*, *116*(A12326), doi:10.1029/2010JA 016792.
- Hoffmann, L., & Alexander, M. J. (2009). Retrieval of stratospheric temperatures
 from atmospheric infrared sounder radiance measurements for gravity wave
 studies. *Journal of Geophysical Research: Atmospheres*, *114*(D7). Retrieved
 from [https://agupubs.onlinelibrary.wiley.com/doi/abs/10.1029/](https://agupubs.onlinelibrary.wiley.com/doi/abs/10.1029/2008JD011241)
[2008JD011241](https://agupubs.onlinelibrary.wiley.com/doi/abs/10.1029/2008JD011241) doi: 10.1029/2008JD011241
- Hoffmann, L., Xue, X., & Alexander, M. J. (2013). A global view of stratospheric
 gravity wave hotspots located with atmospheric infrared sounder observa-
 tions. *J. Geophys. Res. Atmos.*, *118*(2), 416-434. Retrieved from [https://](https://agupubs.onlinelibrary.wiley.com/doi/abs/10.1029/2012JD018658)
agupubs.onlinelibrary.wiley.com/doi/abs/10.1029/2012JD018658 doi:
 10.1029/2012JD018658
- Hólm, E., Forbes, R., Lang, S., Magnusson, L., & Malardel, S. (2016).

- 785 New model cycle brings higher resolution. *ECMWF Newsletter*,
786 [http://www.ecmwf.int/sites/default/files/elibrary/2016/16299-newsletter-](http://www.ecmwf.int/sites/default/files/elibrary/2016/16299-newsletter-no147-spring-2016.pdf)
787 [no147-spring-2016.pdf](http://www.ecmwf.int/sites/default/files/elibrary/2016/16299-newsletter-no147-spring-2016.pdf), 14-19.
- 788 Holton, J. R. (1982). The role of gravity wave induced drag and diffusion in the mo-
789 mentum budget of the mesosphere. *J. Atmos. Sci*, *39*, 791-799.
- 790 Holton, J. R. (1983). The influence of gravity wave breaking on the general circula-
791 tion of the middle atmosphere. *J. Atmos. Sci*, *40*(2497-2507).
- 792 Holton, J. R., & Alexander, M. J. (2000). The role of waves in the transport circula-
793 tion of the middle atmosphere. In G. M. Ser. (Ed.), *Atmospheric science across*
794 *the stratopause*, (Vol. 123, p. 21-35).
- 795 Horinouchi, T., Nakamura, T., & Kosaka, J.-i. (2002). Convectively gener-
796 ated mesoscale gravity waves simulated throughout the middle atmosphere.
797 *Geophysical Research Letters*, *29*(21), 3-1-3-4. Retrieved from [https://](https://agupubs.onlinelibrary.wiley.com/doi/abs/10.1029/2002GL016069)
798 agupubs.onlinelibrary.wiley.com/doi/abs/10.1029/2002GL016069 doi:
799 [10.1029/2002GL016069](https://agupubs.onlinelibrary.wiley.com/doi/abs/10.1029/2002GL016069)
- 800 Jacobi, C. (2012). 6 year mean prevailing winds and tides measured by VHF meteor
801 radar over Collm (51.3N, 13.0E). *J. Atmos. Sol. -Terr. Phys*, *78-79*(8-18).
- 802 Kaifler, B., Kaifler, N., Ehard, B., Dörnbrack, A., Rapp, M., & Fritts, D. C. (2015).
803 Influences of source conditions on mountain wave penetration into the strato-
804 sphere and mesosphere. *Geophys. Res. Lett.*, *42*(21), 9488-9494. Retrieved
805 from [https://agupubs.onlinelibrary.wiley.com/doi/abs/10.1002/](https://agupubs.onlinelibrary.wiley.com/doi/abs/10.1002/2015GL066465)
806 [2015GL066465](https://agupubs.onlinelibrary.wiley.com/doi/abs/10.1002/2015GL066465) doi: 10.1002/2015GL066465
- 807 Kaifler, N., Kaifler, B., Ehard, B., Gisinger, S., Dörnbrack, A., Rapp, M., & Liley,
808 B. (2017). Observational indications of downward-propagating grav-
809 ity waves in middle atmosphere lidar data. *J. Atmos. Sol. Terr. Phys.*,
810 *162*(doi:10.1016/j.jastp.2017.03.003), 16-27.
- 811 Kim, Y.-H., & Chun, H.-Y. (2008). Effects of the basic-state wind on secondary
812 waves generated by the breaking of gravity waves in the mesosphere. *APJASP*,
813 *45* (1), 91-100.
- 814 Kim, Y. J., Eckermann, S. D., & Chun, H. Y. (2003). A overview of the past,
815 present, and future of gravity wave drag parameterization for numerical cli-
816 mate and weather prediction models. *Atmos. Ocean.*, *41*, 65-98.
- 817 Lane, T. P., Reeder, M. J., & Clark, T. L. (2001). Numerical Modeling of Grav-

- ity Wave Generation by Deep Tropical Convection. *J. Atmos. Sci.*, *58*, 1249-1274.
- LeVeque, R. J. (2002). *Finite Volume Methods for Hyperbolic Problems* (No. ISBN-0-521-00924-3). Cambridge Univ. Press.
- LeVeque, R. J., & Berger, M. J. (2004). Clawpack software version 4.6. www.clawpack.org.
- Lindzen, R. S. (1981). Turbulence and stress owing gravity wave and tidal breakdown. *J. Geophys. Res.*, *86*(C10), 9707-9714.
- Lund, T. S., & Fritts, D. C. (2012). Numerical simulation of gravity wave breaking in the lower thermosphere. *J. Geophys. Res.*, *117*(D21105), doi:10.1029/2012JD017536.
- Malardel, S., & Wedi, N. P. (2016). How does subgrid-scale parametrization influence nonlinear spectral energy fluxes in global nwp models? *J. Geophys. Res. Atmos.*, *121*(doi:10.1002/2015JD023970).
- McFarlane, N. A. (1987). The effect of orographically excited gravitywave drag on the general circulation of the lower stratosphere and troposphere. *J. Atmos. Sci.*, *44*, 1775-1800.
- McLandress, C., Shepherd, T. G., Polavarapu, S., & Beagley, S. R. (2012). Is missing orographic gravity wave drag near 60°s the cause of the stratospheric zonal wind biases in chemistry-climate models? *J. Atmos. Sci.*, *69*(3), 802-818. Retrieved from <https://doi.org/10.1175/JAS-D-11-0159.1> doi:10.1175/JAS-D-11-0159.1
- Nappo, C. J. (2002). *An Introduction to Atmospheric Gravity Waves*. Academic, San Diego, California.
- Nastrom, G. D., & Fritts, D. (1992). Sources of mesoscale variability of gravity waves, Part I, Topographic excitation. *J. Atmos. Sci.*, *49*(101-110).
- Piani, C., Durran, D., Alexander, M. J., & Holton, J. R. (2000). A numerical study of three-dimensional gravity waves triggered by deep tropical convection and their role in the dynamics of the QBO. *J. Atmos. Sci.*, *57*, 3689-3702.
- Picone, J. M., Hedin, A. E., Drob, D. P., & Aikin, A. (2002). NRL-MSISE-00 Empirical Model of the Atmosphere: Statistical Comparisons and Scientific Issues. *J. Geophys. Res.*, *107*(A12), SIA 15-1 - SIA 15-16.
- Satomura, T., & Sato, K. (1999). Secondary generation of gravity waves associated

- 851 with the breaking of mountain waves. *J. Atmos. Sci.*, *56*(22), 3847-3858. Re-
 852 trieved from [https://doi.org/10.1175/1520-0469\(1999\)056<3847:SGOGWA>](https://doi.org/10.1175/1520-0469(1999)056<3847:SGOGWA>2.0.CO;2)
 853 [2.0.CO;2](https://doi.org/10.1175/1520-0469(1999)056(3847:SGOGWA)2.0.CO;2) doi: 10.1175/1520-0469(1999)056(3847:SGOGWA)2.0.CO;2
- 854 Senf, F., & Achatz, U. (2011). On the impact of middle-atmosphere thermal tides on
 855 the propagation and dissipation of gravity waves. *J. Geophys. Res.*, *116*(D24),
 856 27.
- 857 Smith, R. B. (1979). The influence of mountains on the atmosphere. *Adv. Geophys.*,
 858 *21*, 87-239.
- 859 Smith, R. B., Nugent, A. D., Kruse, C. G., Fritts, D. C., Doyle, J. D., Eckermann,
 860 S. D., ... Beaton, S. (2016). Stratospheric gravity wave fluxes and scales
 861 during deepwave. *J. Atmos. Sci.*, *73*(7), 2851-2869. Retrieved from [https://](https://doi.org/10.1175/JAS-D-15-0324.1)
 862 doi.org/10.1175/JAS-D-15-0324.1 doi: 10.1175/JAS-D-15-0324.1
- 863 Smith, S. M., Vadas, S. L., Baggaley, W. J., Hernandez, G., & Baumgardner, J.
 864 (2013). Gravity wave coupling between the mesosphere and thermosphere over
 865 new zealand. *J. Geophys. Res. Sp. Phys*, *118*(5), 2694-2707. Retrieved from
 866 <https://agupubs.onlinelibrary.wiley.com/doi/abs/10.1002/jgra.50263>
 867 doi: 10.1002/jgra.50263
- 868 Snively, J., & Pasko, V. P. (2003). Breaking of thunderstorm-generated gravity
 869 waves as a source of short-period ducted waves at mesopause altitudes. *Geo-*
 870 *phys. Res. lett.*, *30*(24).
- 871 Snively, J. B. (2013). Mesospheric hydroxyl airglow signatures of acoustic and
 872 gravity waves generated by transient tropospheric forcing. *Geophys. Res. lett.*,
 873 *40*(doi:10.1002/grl.50886), 1-5.
- 874 Snively, J. B., & Pasko, V. P. (2008). Excitation of ducted gravity waves in the
 875 lower thermosphere by tropospheric sources. *J. Geophys. Res.*, *113*.
- 876 Song, I., Chun, H. Y., & Lane, T. P. (2003). Generation mechanisms of convectively
 877 forced internal gravity waves and their propagation to the stratosphere. *J. At-*
 878 *mos. Sci.*, *60*, 1960-1980.
- 879 Stephan, C., Alexander, M. J., & Richter, J. H. (2016, doi:10.1175/JAS-D-15-
 880 0303.1). Characteristics of gravity waves from convection and implications
 881 for their parameterization in global circulation models. *J. Atmos. Sci.*, *73*,
 882 2729-2742.
- 883 Stober, G., Chau, J. L., Vierinen, J., Jacobi, C., & Wilhelm, S. (2018,

- 884 <https://doi.org/10.5194/amt-11-4891-2018>). Retrieving horizontally resolved
885 wind fields using multi-static meteor radar observations. *Atmos. Meas. Tech.*,
886 *11*, 4891–4907.
- 887 Stober, G., Matthias, V., Jacobi, C., Wilhelm, S., Höffner, J., & Chau, J. L.
888 (2017). Exceptionally strong summer-like zonal wind reversal in the up-
889 per mesosphere during winter 2015/16. *Ann. Geophys.*, *35*(3), 711–720.
890 Retrieved from <https://www.ann-geophys.net/35/711/2017/> doi:
891 10.5194/angeo-35-711-2017
- 892 Torrence, C., & Compo, G. P. (1998). A practical guide to wavelet analysis. *Bull.*
893 *Am. Met. Soc.*, *79*(1).
- 894 Vadas, S. L. (2007). Horizontal and vertical propagation and dissipation of gravity
895 waves in the thermosphere from lower atmospheric and thermospheric sources.
896 *J. Geophys. Res.*, *112*(A06305).
- 897 Vadas, S. L., & Becker, E. (2019). Numerical modeling of the generation of
898 tertiary gravity waves in the mesosphere and thermosphere during strong
899 mountain wave events over the southern andes. *Journal of Geophysical*
900 *Research: Space Physics*, *124*(9), 7687–7718. Retrieved from [https://](https://agupubs.onlinelibrary.wiley.com/doi/abs/10.1029/2019JA026694)
901 agupubs.onlinelibrary.wiley.com/doi/abs/10.1029/2019JA026694 doi:
902 10.1029/2019JA026694
- 903 Vadas, S. L., & Crowley, G. (2010). Sources of the traveling ionospheric distur-
904 bances observed by the ionospheric tiddbit sounder near wallops island on
905 30 october 2007. *Journal of Geophysical Research: Space Physics*, *115*(A7).
906 Retrieved from [https://agupubs.onlinelibrary.wiley.com/doi/abs/](https://agupubs.onlinelibrary.wiley.com/doi/abs/10.1029/2009JA015053)
907 [10.1029/2009JA015053](https://agupubs.onlinelibrary.wiley.com/doi/abs/10.1029/2009JA015053) doi: 10.1029/2009JA015053
- 908 Vadas, S. L., & Fritts, D. C. (2005). Thermospheric responses to gravity waves:
909 Influences of increasing viscosity and thermal diffusivity. *J. Geophys. Res.*,
910 *110*(D15103).
- 911 Vadas, S. L., Fritts, D. C., & Alexander, M. J. (2003). Mechanism for the Gener-
912 ation of Secondary Waves in Wave Breaking Regions. *J. Atmos. Sci.*, *60*, 194-
913 214.
- 914 Vadas, S. L., Liu, H.-L., & Lieberman, R. S. (2014). Numerical modeling of the
915 global changes to the thermosphere and ionosphere from the dissipation of
916 gravity waves from deep convection. *J. Geophys. Res. Sp. Phys.*, *119*(9), 7762-

7793. Retrieved from <https://agupubs.onlinelibrary.wiley.com/doi/abs/10.1002/2014JA020280> doi: 10.1002/2014JA020280
- Vadas, S. L., Xu, S., Yue, J., Bossert, K., Becker, E., & Baumgarten, G. (2019). Characteristics of the quiet-time hot spot gravity waves observed by goce over the southern andes on 5 july 2010. *J. Geophys. Res .Sp. Phys*, 124(<https://doi.org/10.1029/2019JA026693>).
- Vadas, S. L., Zhao, J., Chu, X., & Becker, E. (2018). The excitation of secondary gravity waves from body forces: Theory and observation. *J. Geophys. Res. Atmos.*, 123. Retrieved from <https://agupubs.onlinelibrary.wiley.com/doi/abs/10.1029/2017JD027970> doi: 10.1029/2017JD027970
- Yiğit, E., & Medvedev, A. S. (2015). Internal wave coupling processes in Earth's atmosphere. *Adv. Space Res.*, 55(doi: 10.1016/j.asr.2014.11.020.).
- Zettergren, M. D., & Snively, J. B. (2015). Ionospheric response to infrasonic-acoustic waves generated by natural hazard events. *J. Geophys. Res .Sp. Phys*, 120(9), 8002–8024. Retrieved from <http://dx.doi.org/10.1002/2015JA021116> (2015JA021116) doi: 10.1002/2015JA021116
- Zhou, X., Holton, J. R., & Mullendore, G. L. (2002). Forcing of secondary waves by breaking of gravity waves in the mesosphere. *J. Geophys. Res. Atmos.*, 107(D7), ACL 3-1-ACL 3-7. Retrieved from <https://agupubs.onlinelibrary.wiley.com/doi/abs/10.1029/2001JD001204> doi: 10.1029/2001JD001204